Infrared-active excitations in tunneling superlattices and d-parameter theory

Jian Zhang and Sergio E. Ulloa
Department of Physics and Astronomy and Condensed Matter and Surface Sciences Program, Ohio University, Athens, Ohio 45701-2979
William L. Schaich
Department of Physics, Indiana University, Bloomington, Indiana 47405
(Received 21 November 1990)

We present a theoretical study of the far-infrared response of doped tunneling superlattices using the d-parameter formalism. The $d(\omega)$ functions provide both the position and coupling strengths of all possible infrared-active modes in the superlattices and our model calculations reveal single-particle-like transitions as well as intraminiband and interminiband plasma modes. A series of surface excitations, related to charge depletion in the end layers of real tunneling superlattices, are distinguishable from the corresponding bulk modes. The spatial variation of the induced charge density in these additional modes is quite different from that of the bulk modes. The surface-mode energies are sensitive to details of the depletion-density profiles, which in turn are easily modified by an applied gate voltage, thereby shifting the surface absorption frequencies.

I. INTRODUCTION

Developments in molecular-beam epitaxy have made possible the growth of high-quality GaAs-$Al_xGa_{1-x}As$ superlattices with abrupt interfaces and very thin layers.[1] At the simplest (idealized) level, one can view the layers as identical, uncoupled, and extending forever along the growth axis. However, real systems are of finite length and (if the layers are thin enough) allow tunneling of charge carriers between layers as well as nearly free motion within layers. In addition to this three-dimensional (but anisotropic) conduction, the near-surface layers differ from those in the bulk by having a reduced, position-dependent charge density. These carrier-depletion regions are due to semiconductor surface states (associated with dangling bonds, defects, and impurities) which provide a reservoir of electronic traps near the ends of the superlattice and strongly pin the Fermi level to the semiconductor midgap. The net result is that finite doped superlattices possess considerable anisotropy and inhomogeneity, which, on the one hand, can be conveniently modified by growth conditions and gate voltages to tailor the system's response but, on the other hand, present a considerable challenge to theory for a quantitative description.

Self-consistent calculations of the electronic-level structure in such systems have been presented earlier[2-7] and we use these results here to build a theory of infrared absorption. Brief reports of our initial results have already been published.[8,9] Although there have been numerous theoretical papers discussing plasmons in superlattices,[10-22] none of them considers simultaneously all the complications noted above. The previous work has also been mainly directed towards inelastic light scattering since experimental studies of superlattices using that probe are available.[23-27] We have chosen to examine infrared absorption because it represents a complementary experimental probe and because it provides an interesting application of the d-parameter formalism, which was originally developed to describe nonlocal screening effects at the surface of clean (jellium) metals.[28-31] This theory has had several recent successes[32,33] and calculations can now be done at a fairly sophisticated level.[34] The original formalism has been generalized,[35-37] opening up a wide range of potential applications[38,39] and in addition the essential equivalence of this approach to several alternative formalisms has been established.[36,39] For finite superlattice systems, we will show that the $d(\omega)$ functions yield the excitation strengths and energy positions for all possible infrared absorptions.

After a brief overview of this approach, we derive in Sec. II the equations necessary for its application. This is done at various levels of sophistication, ranging from imagining the superlattice response to be given by scaling down (to less than a micrometer in length) the bulk response of a very long superlattice to including the self-consistent interaction of excitations from and to both bulk (but finite sized) and surface (Tamm) states in the realistic inhomogeneous system. Then in Sec. III a series of model calculations are presented illustrating the possible spectra and their physical content. As expected in the long-wavelength limit, intraminiband and interminiband plasma modes carry most of the excitation strength, although interminiband excitations with a predominant single-particle character are also present with significant

weight. One can distinguish surface from bulk modes in the absorption spectrum and we discuss their different behaviors with respect to variations in structural and other parameters. Finally in Sec. IV we sumarize our calculations and compare their evaluations and content to inelastic light or electron scattering.

II. FORMULATION

A. *d*-parameter formalism

We shall treat a semiconductor superlattice as N quantum wells separated by finite potential barriers and immersed in a semi-infinite ($z \geq 0$) uniform medium of (local) dielectric function ϵ. Since the superlattice structures we consider are less than a micrometer in total length, it is reasonable to view these electronic multilayer systems as a surface modification of the substrates on which they are deposited, given that the excitations of interest only absorb light whose wavelength is much greater than the superlattice thickness. In this long-wavelength regime one can describe the changes in the optical behavior of the surface due to the superlattice by d parameters in a spirit similar to the study of adsorbate-layer systems.[38,39]

Consider first light incident from vacuum on the flat surface of a uniform substrate characterized by ϵ. If ω is the light frequency and θ the angle of incidence with respect to the surface normal, then

$$Q = \frac{\omega}{c}\sin\theta \tag{1}$$

is the projection of the incident wave vector on the surface plane and

$$p_v = \frac{\omega}{c}\cos\theta \tag{2}$$

is its normal component in vacuum. Both the reflected and transmitted beams have the same wave-vector projection in the surface plane as (1), but their normal components differ from (2). That for the reflected wave is simply $-p_v$ while the transmitted wave has[40]

$$p_m = \left(\frac{\omega^2}{c^2}\epsilon - Q^2\right)^{1/2}, \tag{3}$$

which in general is complex valued. One should use the root that makes the imaginary part of p_m positive. The Fresnel predictions for reflection and transmission amplitudes of the electric field are determined by ϵ and the wave-vector components (2) and (3). Their explicit form depends on the polarization of the incident wave, which, like Q, is preserved through the interaction process for a flat interface. If the electric field vector lies in the plane of incidence (p polarization), one has, from classical optics,

$$r_0 = \frac{p_v\epsilon - p_m}{p_v\epsilon + p_m}, \tag{4}$$

$$t_0 = \frac{2p_v}{p_v\epsilon + p_m}, \tag{5}$$

where we have used a subscript 0 for these Fresnel answers.

Next one can ask how these equations change if the optical response of a thin region near the surface is modified. In the limit that the thickness of this region is small compared with c/ω and the inverses of (1)–(3), the modified reflection and transmission amplitudes can be expressed (again for p polarization) as[36]

$$r = \frac{p_v\epsilon - p_m - ip_v(1-\epsilon)(p_m d_{\|} - Q^2 d_{\perp}/p_v)}{p_v\epsilon + p_m - ip_v(1-\epsilon)(p_m d_{\|} + Q^2 d_{\perp}/p_v)}, \tag{6}$$

$$t = \frac{2p_v}{p_v\epsilon + p_m - ip_v(1-\epsilon)(p_m d_{\|} + Q^2 d_{\perp}/p_v)}, \tag{7}$$

where the only additional quantities are the two d parameters $d_{\|}$ and $d_{\perp}$, which are complex-valued functions of frequency with units of length. It is important to remark that the d's do not depend on θ or on any of the wave-vector components in (1)–(3). Hence the angular variation of r and t is easily found from that of Q, p_v, and p_m. The appearance of only two d functions in (6) and (7) is a consequence of the presumed symmetry of the system: the growth axis of the superlattice is along the surface normal and each layer has a (two-dimensional) isotropy and translational invariance.

This isotropy and homogeneity for motion parallel to the surface makes $d_{\|}$ easy to find. It is formally given by the integral along the surface normal

$$(1-\epsilon)\,d_{\|} = \int_0^{\infty} dz[\epsilon_{\|}(z) - \epsilon], \tag{8}$$

where the difference between $\epsilon_{\|}(z)$ and ϵ is determined by the extra conductivity due to the carriers in the superlattice moving parallel to the surface, which in turn is well approximated by a Drude expression. Thus

$$\epsilon_{\|}(z) - \epsilon = \frac{4\pi i}{\omega}\sigma_{\|}(z) \tag{9}$$

with

$$\sigma_{\|}(z) = \frac{in(z)e^2/m}{\omega + i/\tau}, \tag{10}$$

where ω is the driving frequency, $n(z)$ the equilibrium (three-dimensional) carrier density, m an effective mass, and $1/\tau$ a (transport) scattering rate. Combining (8)–(10) we obtain

$$(1-\epsilon)\,d_{\|} = -\frac{4\pi N_s e^2/m}{\omega(\omega + i/\tau)}, \tag{11}$$

where

$$N_s = \int_0^{\infty} dz\, n(z) \tag{12}$$

is the total (two-dimensional) density of carriers in the superlattice. In the limit of long-wavelength perturbations the current response parallel to the surface involves negligible phase differences between different lay-

ers within the superlattice. Hence the currents induced by an electric field parallel to the surface can be simply lumped into an effective current sheet involving N_s.

This physical interpretation is more evident if we use $\sigma_s = \int dz\, \sigma_{||}(z)$ instead of $d_{||}$ in (6) and (7). For instance, rewriting (7) for the case of normal incidence (so $Q = 0$ and $d_\perp$ is irrelevant) yields

$$t(\theta = 0) = \frac{2/\sqrt{\epsilon}}{1 + \sqrt{\epsilon} + \frac{4\pi}{c}\sigma_s} , \tag{13}$$

which shows the classical reduction of t_0 due to a current sheet of conductance σ_s.

A perhaps more interesting consequence of the $d_{||}$ of (11) occurs on the other side of the light line; i.e., for $Q > \omega/c$, which can be realized, say, by using a prism coupler near the surface in a frustrated total reflection geometry. To find a simple result, we imagine $Q >> \omega/c$ so both p_v and p_m may be replaced by iQ. Then the denominators in (6) and (7) will vanish when

$$\omega^2 = \frac{4\pi N_s e^2 Q}{m(\epsilon + 1)} , \tag{14}$$

where we have neglected both $1/\tau$ and $d_\perp$. The resulting singular structure in r and t thus occurs along the dispersion of the (nonretarded) two-dimensional plasmon of a charge sheet characterized by N_s and m and located on the surface plane of the substrate.

The calculation and interpretation of $d_\perp$ are much more involved. Before plunging into details, consider how the influence of $d_\perp$ would appear in experiments. One might be looking for small changes in the reflection coefficient, $R = |r|^2$, or the transmission coefficient, $T = |t\sqrt{\epsilon}|^2\sqrt{\epsilon}$, due to excitations in the superlattice. Expanding (6) and (7) we find to first order in the d's [which is the limit of formal validity of (6) and (7) (Ref. 36)] for the relative changes in R and T

$$\Delta R/R \approx -4p_v \mathrm{Im}\left(d_{||} + \frac{Q^2\epsilon(d_{||} - d_\perp)}{\epsilon p_v^2 - Q^2}\right) , \tag{15}$$

$$\Delta T/T \approx 2p_v \mathrm{Im}\left(\frac{\epsilon - 1}{\epsilon p_v + p_m}(p_m d_{||} + Q^2 d_\perp/p_v)\right) , \tag{16}$$

where Im denotes "imaginary part of." The value of (15) and (16) is that they provide explicit relations between measureable quantities, $\Delta R/R$ and $\Delta T/T$, and calculable quantities, $d_\perp$ and $d_{||}$. Hence our numerical estimates of the d's can be readily converted into predictions of signal strengths, or vice versa. This utility of the d's continues to hold true for more complicated geometries than considered here, as long as the influence of the superlattice can be treated as a small perturbation on the overall optical response. One need only solve the system optics first using r_0 and t_0 at the interface where the superlattice will reside, and then substitute a first-order expansion of r and t into the final results.

B. Formulas for $d_\perp$

A general equation for $d_\perp$ due to a finite superlattice is[36]

$$(1 - 1/\epsilon)d_\perp = \int_0^\infty dz \int_0^\infty dz' [\, \epsilon_\perp^{-1}(z, z') - (1/\epsilon)\delta(z - z')] \tag{17}$$

where we have allowed for nonlocality in the response along the growth axis. If we neglect this feature, (17) reduces to a close analog of (8):

$$(1 - 1/\epsilon)\, d_\perp \approx \int_0^\infty dz\, [1/\epsilon_\perp(z) - 1/\epsilon] . \tag{18}$$

However, the jump from (17) to (18) is a quantitatively important approximation due to the system's strong inhomogeneity along z. Hence we return to (17) and reexpress it as

$$d_\perp = \frac{4\pi e}{1 - \epsilon} \int_0^\infty dz\, z\, \Delta\rho(z)/D_\perp(0) , \tag{19}$$

where $\Delta\rho(z)$ is the induced carrier density and $D_\perp(0)$ is the (essentially constant) normal component of the displacement field of a long-wavelength perturbation. We calculate $\Delta\rho(z)$ from the linear response formula

$$\Delta\rho(z) = \int_0^\infty \chi(z, z'; \omega) V_{\mathrm{ext}}(z')\, dz', \tag{20}$$

where the perturbing potential energy seen by the superlattice, which is embedded in the dielectric, is

$$V_{\mathrm{ext}}(z) = -ezD_\perp(0)/\epsilon . \tag{21}$$

The susceptibility χ is found in a mean-field approximation by solving

$$\chi(z, z') = \chi_0(z, z') + \int\int \chi_0(z, \overline{z}) V(\overline{z}, \overline{z}') \chi(\overline{z}', z')\, d\overline{z}\, d\overline{z}', \tag{22}$$

where χ_0 is the independent-particle susceptibility and various terms can be included in the interaction potential energy $V(z, z')$. At the simplest (random-phase approximation, RPA) level one keeps only the direct Coulomb (Hartree) interaction and an image term:

$$V \approx V_H + V_I , \tag{23}$$

where

$$V_H(z, z') = -\frac{2\pi e^2}{\epsilon}|z - z'| \tag{24}$$

and

$$V_I(z, z') = -\frac{2\pi e^2}{\epsilon}\frac{\epsilon - 1}{\epsilon + 1}(z + z') . \tag{25}$$

However, the latter term produces no net effect, since in the present long-wavelength limit its integral with $\Delta\rho(z')$ yields only a position-independent result because there is no net induced carrier charge: $\int_0^\infty dz'\, \Delta\rho(z') = 0$.

To calculate χ_0 requires a description of the single-particle structure of the superlattice. We assume free motion (with an effective mass) in the x-y plane and tunneling motion along z. An electronic eigenfunction is written as

$$\Psi_{n,\mathbf{k_t}}(\mathbf{r_{xy}},z)=\frac{1}{\sqrt{A}}\exp(i\mathbf{k_t}\cdot\mathbf{r_{xy}})\Phi_n(z), \tag{26}$$

where A is a quantization area and $\Phi_n(z)$ is expanded in a Wannier representation

$$\Phi_n(z)=\sum_{i,\alpha} b^n_{i\alpha}\phi^\alpha_i(z), \tag{27}$$

with $\phi^\alpha_i(z)$ the Wannier function for the αth miniband centered on the ith layer. The eigenvalue associated with the product state (26) is

$$E_{n,\mathbf{k_t}}=E_n+\hbar^2\mathbf{k}_t^2/2m. \tag{28}$$

The energy-level structure $\{E_n\}$ and associated eigenvectors $\{b^n_{i\alpha}\}$ can be obtained from the tunneling Hamiltonian for the superlattice, given in a tight-binding approximation by

$$H_z=\sum_{j,\alpha}[\,(e_\alpha+v_j)C^\dagger_{j,\alpha}C_{j,\alpha}-t_\alpha C^\dagger_{j+1,\alpha}C_{j,\alpha} -t_\alpha C^\dagger_{j,\alpha}C_{j+1,\alpha}]+\sum_{j,\alpha\neq\alpha'}U_{j,\alpha,\alpha'}C^\dagger_{j,\alpha}C_{j,\alpha'}, \tag{29}$$

where $C_{j,\alpha}$ is the destruction operator associated with the Wannier state ϕ^α_i, the t_α are the nearest-neighbor hopping matrix elements for each band, and the e_α are related to the energy minigap parameters. The term with $U_{j,\alpha,\alpha'}$ represents the miniband mixing induced by the gradient of the inhomogeneous self-consistent potential, v_j, which in turn takes into account the electron–donor-ion and electron-electron interactions in a Hartree approximation. (Exchange effects are discussed below in Secs. II C and III D.) The inhomogeneous potential obeys Poisson's equation with boundary conditions which simulate the effects of the Fermi-level pinning producing charge depletion in a realistic superlattice. Further details of the calculation of the level structure and eigenfunctions can be found elsewhere.[4,5,7]

The ingredients (27) and (28) determine $\chi_0(z,z')$ through

$$\chi_0(z,z')=\sum_{n,n'}\Pi_{n,n'}\Phi_n(z)\Phi_{n'}(z)\Phi_n(z')\Phi_{n'}(z') =\sum_{s,s'}A_s(z)\mathbf{B}_{ss'}A_{s'}(z'), \tag{30}$$

with

$$A_s(z)=\phi^\alpha_i(z)\phi^\beta_j(z), \tag{31}$$

$$\mathbf{B}_{ss'}=\sum_{n,n'}b^n_{i\alpha}b^{n'}_{j\beta}\Pi_{n,n'}b^n_{i'\alpha'}b^{n'}_{j'\beta'}, \tag{32}$$

and

$$\Pi_{n,n'}=N_n\frac{2(E_n-E_{n'})}{(E_n-E_{n'})^2-\hbar\omega(\hbar\omega+i\gamma)}. \tag{33}$$

Here s is a compound index which stands for (i,α,j,β) and γ is a phenomenological damping parameter which takes into account the impurity broadening of levels. The factor

$$N_n=\frac{m}{\pi\hbar^2}(E_F-E_n)\,f_n\ , \tag{34}$$

with the Fermi energy E_F, is an effective two-dimensional density associated with the nth state for motion along z, and f_n is the Fermi factor for that level.

The Wannier representation makes it possible to decouple and solve the mean-field equation (22) exactly.[41,42] We obtain

$$\chi(z,z';\omega)=\sum_{s,s'}A_s(z)[\mathbf{B}(\mathbf{1}-\mathbf{VB})^{-1}]_{ss'}A_{s'}(z'), \tag{35}$$

where

$$\mathbf{V}_{ss'}=\int\int A_s(z)V(z,z')A_{s'}(z')\,dz\,dz'. \tag{36}$$

Correspondingly, the induced carrier density in Eq. (20) can be written as

$$\Delta\rho(z,\omega)=-\frac{e}{\epsilon}D_\perp(0)\sum_{s,s'}A_s(z)[\mathbf{B}(\mathbf{1}-\mathbf{VB})^{-1}]_{ss'}H_{s'}, \tag{37}$$

where $H_s=\int zA_s(z)\,dz$ is a dipole matrix element between Wannier functions. Finally, combining Eqs. (19) and (37) leads to the convenient expression

$$d_\perp=\frac{4\pi e^2}{\epsilon(\epsilon-1)}\sum_{s,s'}H_s[\mathbf{B}(\mathbf{1}-\mathbf{VB})^{-1}]_{ss'}H_{s'}, \tag{38}$$

which is the basis of the numerical calculations described in Sec. III. The explicit form of the Wannier functions used in the evaluation of the various matrix elements in these expressions is obtained from the numerical solution of a Kronig-Penney problem with appropriate parameters; see the Appendix for details. The definite-parity and highly localized behavior of the various ϕ^α_i, which results from carefully fixing the phases of the Bloch wave functions,[43] greatly simplifies calculations of the matrix elements $\mathbf{B}_{ss'}$ and $\mathbf{V}_{ss'}$. For instance, it suffices to include no further than nearest neighbors in the calculation of elements of $\mathbf{V}_{ss'}$.

To end this subsection we remark that in a polar material like GaAs and over the frequency range of interest, the optical phonons are active and should not be ignored. This effect, however, is reasonably treated by simply making the background ϵ frequency dependent according to

$$\epsilon(\omega) = \epsilon_\infty \frac{\omega^2 - \omega_L^2 + i\gamma_{ph}\omega}{\omega^2 - \omega_T^2 + i\gamma_{ph}\omega}, \tag{39}$$

where ω_T and ω_L are the transverse and longitudinal optical-phonon frequencies, respectively. We use for the parameters in (39) $\hbar\omega_T = 33.6$ meV, $\hbar\omega_L = 36.8$ meV, $\epsilon_\infty = 10.4$, and $\hbar\gamma_{ph} = 1$ meV.[13,17,18,20] For qualitative insights we occasionally keep just the static limit of (39), where $\epsilon(\omega \to 0) \to \epsilon_0 = 12.5$.

C. Excitonic effects

It is well known in the study of strongly interacting systems that the Hartree approximation overestimates the effect of Coulomb repulsion between carriers, which exchange and correlation effects tend to compensate.[44] Beginning with the work of Ando on quantum wells[45] it has been realized that this countering of Coulomb effects in the optical response of systems with reduced dimensionality can be substantial. In order to estimate its effect on the various excitation modes for our system, we use a local-density approximation for the exchange energy functional, as has been done before in the study of other heterojunction and superlattice systems.[13,17,18,20]

First, we include the exchange potential v^x in the z-motion Hamiltonian of Eq. (29) by adding a term to the local potential v_j of the form

$$v_j^x = -\frac{e^2}{\pi\epsilon}(3\pi^2\rho_j/a)^{1/3}, \tag{40}$$

where ρ_j is the electron areal density in well j and a is the superlattice period. The resulting electronic-level structure shows, however, no significant change with respect to previously obtained results (shifts of less than 0.2 meV).[5,9]

More important is the incorporation of exchange effects into the dynamical response function of the system.[45] These are included in our calculation by adding a term to the two-dimensional interaction potential of Eq. (23) of the form.[13,17,18,20,44]

$$V^x(z,z') = \frac{\partial v^x}{\partial n}\delta(z-z'), \tag{41}$$

where n is the effective three-dimensional local electron density ($\simeq \rho_j/a$). The corresponding matrix elements $\mathbf{V}_{ss'}$ in Eq. (36) have an additional exchange term given by

$$\mathbf{V}_{ss'}^x = -\frac{e^2}{3\pi\epsilon}(3\pi^2a^2)^{1/3}\sum_l \rho_l^{-2/3}\mathbf{C}_{ss'}^l, \tag{42}$$

where the density weights are integrated over one superlattice period to account for the discretization of the problem,

$$\mathbf{C}_{ss'}^l = \int_{(l-1/2)a}^{(l+1/2)a} A_s(z)A_{s'}(z)\,dz. \tag{43}$$

Most matrix elements $\mathbf{C}_{ss'}^l$ are small due to the well-localized character of the Wannier functions (see the Appendix). Results of including this interaction will be discussed in Sec. III D below. However, for simplicity, and because we will show them to be unimportant, we will ignore the effects of both v_j^x and $\mathbf{V}_{ss'}^x$ until that section.

D. d parameters in a continuum limit

In order to provide a natural comparison with the behavior of a finite system with depleted end layers, we consider approximate evaluations of (18). At the simplest level one could cut off the z integral at $L \cong Na$ and replace $\epsilon_\perp(z)$ with $\epsilon + \delta\epsilon_\perp$. A further approximation would then be to guess a functional form for the frequency dependence of the (bulk) superlattice contribution, $\delta\epsilon_\perp$, introducing thereby various transition and plasma frequencies, oscillator strengths, etc., to represent the presumed spectrum of optical response. Most of these parameters can be reasonably estimated if we use the model set up here for a finite superlattice to calculate the (local) dielectric function of an infinite superlattice.

To carry through such a calculation we keep only the e_α and t_α terms in (29) and extend the sum on j to infinity. Imposing periodic boundary conditions allows us to write the wave functions for the tunneling motion in the simple form

$$\Phi_{\alpha,k}(z) \propto \sum_j e^{ikja}\phi_j^\alpha(z), \tag{44}$$

such that the corresponding eigenvalues for a two-miniband model are (to within a constant shift)

$$E_1(k) = \frac{\Delta_1}{2}[1-\cos(ka)], \tag{45}$$

$$E_2(k) = E_{gap} + \Delta_1 + \Delta_2 - \frac{\Delta_2}{2}[1-\cos(ka)], \tag{46}$$

where Δ_1 ($= 4t_1$) and Δ_2 ($= -4t_2$) are the (positive) bandwidths and E_{gap} is the miniband gap. The Bloch wave vector k runs between $\pm\pi/a$. Ignoring local-field effects, the electronic contributions to the long-wavelength dielectric response is given in this continuum model by[46]

$$\delta\epsilon_\perp(\omega) = -\frac{2e^2}{\pi}\frac{m}{\hbar^2}\int_{-\pi/a}^{\pi/a} dk \frac{(\partial E_1/\partial k)^2}{(\hbar\omega)^2} - 2e^2\int_{-\pi/a}^{\pi/a} dk\,\Pi(k)\,|S(k)|^2, \tag{47}$$

where we have assumed that the Fermi energy lies in the miniband gap; i.e., $0 < E_F - \Delta_1 < E_{gap}$. The first term is due to intraminiband processes and integrates to

$$\delta\epsilon_\perp^{(intra)}(\omega) = -\frac{\Delta_1^2 ame^2}{2\hbar^4\omega^2}. \tag{48}$$

The second term is from interminiband excitations and involves

$$\Pi(k) = N(k)\frac{2[E_1(k)-E_2(k)]}{[E_1(k)-E_2(k)]^2 - \hbar\omega(\hbar\omega + i\gamma)}, \tag{49}$$

with

$$N(k) = \frac{m}{\pi\hbar^2}\left[E_F - E_1(k)\right] \tag{50}$$

an effective two-dimensional density analogous to the N_n of (34) and

$$S(k) = \sum_j e^{ikja} < \phi_0^1|z|\phi_j^2 > , \tag{51}$$

where the sum on j converges quickly. The k integral of these factors is numerically straightforward, yielding a $\delta\epsilon_\perp^{(\text{inter})}(\omega)$.

Finally one substitutes into (18) to obtain

$$d_\perp = L\left(\frac{1}{\epsilon + \delta\epsilon_\perp} - \frac{1}{\epsilon}\right)\left(1 - \frac{1}{\epsilon}\right)^{-1} \tag{52}$$

whose frequency dependence is easily related to that of ϵ and $\delta\epsilon_\perp$. For example, there are (bulk) plasmon contributions from the zeros of $\epsilon + \delta\epsilon_\perp$ and (52) describes (approximately) both their location and strength. Comparisons with the simple results from (52) will aid the understanding of the complex spectrum predicted by (38).

III. RESULTS AND DISCUSSION

We have calculated d parameters for an n-type doped semiconductor superlattice with typical structural parameters using the various expressions derived in Sec. II. The superlattice structures we have in mind consist of N periods deposited on an undoped buffer layer ($\approx$ 1100 Å) which in turn is followed by a semi-infinite dielectric substrate. We present explicit calculations for $N = 10$ and 20, in a GaAs-AlGaAs system such that $m/m_e = 0.067$, and a = 188 (well) + 38 (barrier) Å= 226 Å, with various bandwidths Δ_1 and Δ_2 (achieved experimentally by varying the Al concentration which changes the potential barrier height). The configuration chosen and some of the parameter values model a system similar to those used in recent quantum Hall-effect experiments.[47]

The ground-state energy-level structure and wave functions for the different systems were obtained using the tight-binding envelope-function approximation described above, where the potential associated with the inhomogeneous charge-depletion regions is incorporated self-consistently for a two-miniband model.[5,7–9] The Fermi-level pinning which produces the depletion regions at the ends of the superlattice gives rise to surface-localized states lying in the miniband midgap with wave functions strongly peaked in one period and with a fast-decaying tail. For the doping densities used ($\rho_+ \simeq 1.9 \times 10^{17}$ cm^{-3}), the Fermi level lies within the miniband gap and only the first z-motion miniband is occupied in the periodic undepleted system. In the case of Fermi-level pinning, however, the corresponding depletion regions extend over two layers on the buffer end and over four layers at the free end. As more layers are added, they join the "bulk" region, and affect very little the extension and energetics of the depletion regions (as long as $N \geq 7$). The resulting surface-localized states (shown as dashed lines in Fig. 1) are related to the depletion regions. They lie close to the Fermi level, but detached from the main group of levels (the remnant of the miniband in this small system with few energy levels), and are very sensitive to the conditions of the surface, such as an applied gate voltage.[2–9] Figure 1 shows the electronic-level structure (with respect to the Fermi level) plotted versus a gate voltage applied across the superlattice. As mentioned before, the exchange-potential term has a negligible effect on the levels on this energy scale. The presence of a gate voltage is simulated by varying the values of the surface-potential parameter appearing in the boundary conditions. For simplicity, we have kept one end of the superlattice fixed, modeling the application of a gate voltage to the "free" end of the structure (where now a gate probe is attached). As shown in Fig. 1, the surface-localized states associated with the depletion region near the free end are drastically shifted down in energy as the gate voltage is increased. Simultaneously, the extension of the corresponding wave function is greatly increased, changing the character of the level from surface localized to bulklike.[2–9]

Possessing now the ground-state levels and wave functions we can proceed to calculate the optical response of the system using d parameters. The various excitation features are described in what follows, beginning with those common to all superlattice systems, with and without depletion regions taken into consideration. We then discuss the excitations unique to systems with depletion regions, where the surface-localized states play an important role. To emphasize the significance of different features appearing in the more realistic (although complex) model, we present in Fig. 2 the functions $d_\perp(\omega)$

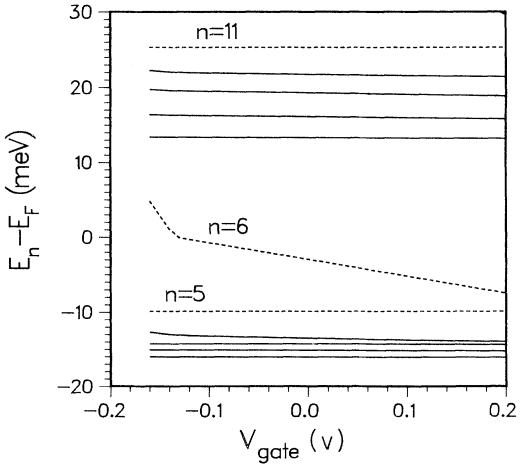

FIG. 1. z-motion electronic states E_n vs gate voltage, plotted with respect to the Fermi level E_F, in a system with ten periods. Notice surface-localized states, dashed lines, detached from miniband level groups. $\rho_+ = 1.9 \times 10^{17}$ cm^{-3}, $\Delta_1 = 2.48$ meV, $\Delta_2 = 10.4$ meV, and $E_{\text{gap}} = 26.2$ meV.

for the various model superlattice systems. The resulting individual features are identified and discussed below according to the different physical characteristics of each mode. Notice that the real and imaginary parts of $d_\perp$ obey a Kramers-Kronig relation, such that the collective modes of the system are characterized by a peak in $\mathrm{Im}(d_\perp)$, occurring simultaneously with a zero in $\mathrm{Re}(d_\perp)$.

A. Intraminiband plasmons

We begin with Fig. 2(a) which shows $d_\perp$ for a uniformly charged (no depletion regions) "bulk" superlattice, with structure parameters as specified above and Δ_1, Δ_2, and E_{gap} given by 2.48, 10.42, and 26.2 meV, respectively (corresponding approximately to a GaAs–$Al_{0.18}Ga_{0.82}As$ system with a barrier height of 134 meV).[47] The curves in Fig. 2(a) have been obtained from Eq. (52) with $\epsilon = \epsilon_0 = 12.5$ and $E_F = 16.6$ meV (corresponding to $N_s/N = \rho_+ a$). The first peak in the imaginary part of $d_\perp$ (at 2.5 meV) corresponds to the so-called intraminiband plasmon. This identification can be verified by looking for the zero of $\epsilon_0 + \delta\epsilon_\perp^{(\mathrm{intra})}(\omega)$ at low frequencies, where $\delta\epsilon_\perp^{(\mathrm{inter})}(\omega)$ has been neglected. In that case, the intraminiband plasma frequency is given by

$$\omega_{\mathrm{intra}} = \left(\frac{me^2a}{2\epsilon\hbar^4}\right)^{1/2}\Delta_1, \tag{53}$$

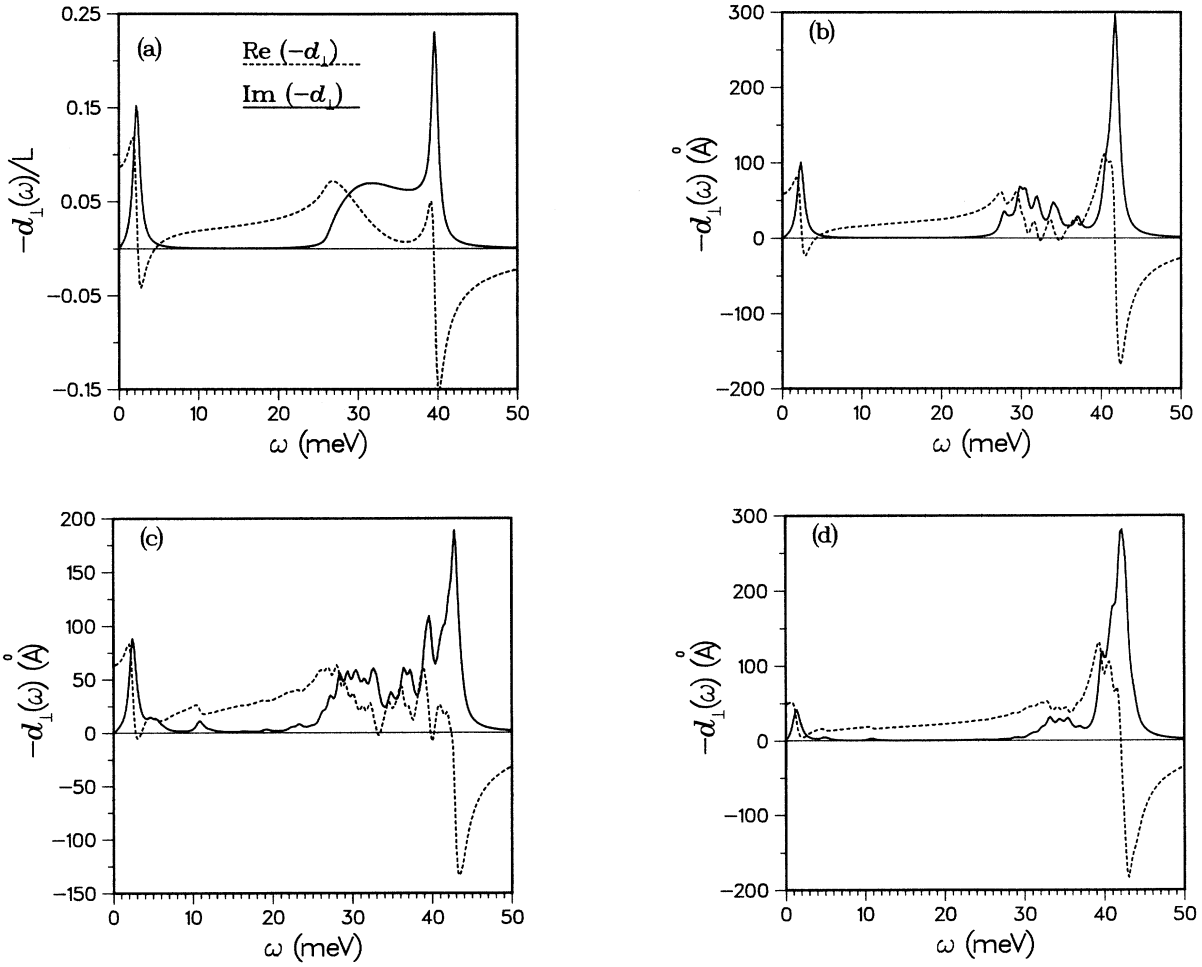

FIG. 2. $d_\perp$ plotted vs frequency for (a) piece of "bulk" superlattice with band structure parameters as in Fig. 1; (b) finite superlattice with same parameters and *homogeneous* charge distribution, five periods; (c) finite, ten-period superlattice with same parameters *and* charge depletion in the surface regions (energy levels in Fig. 1 for $V_{\mathrm{gate}} = 0$); (d) ten-period superlattice with charge depletion and parameters $\Delta_1 = 1.24$ meV, $\Delta_2 = 5.2$ meV, $E_{\mathrm{gap}} = 31$ meV, and same period $a = 226$ Å. $\gamma = 1$ meV in all plots. Real (imaginary) part of $d_\perp$ shown as dashed (solid) lines.

as presented previously.[10,22] The tunneling motion in the z direction allows for intraminiband plasmons in the long-wavelength limit such that the plasma frequency is proportional to the miniband width, in contrast with the situation of a purely two-dimensional system where the plasma frequency vanishes for $Q \to 0$.[10,22] This result can also be viewed as the remnant in an anisotropic three-dimensional (3D) system of the well-known finite value of the plasma frequency in the long-wavelength limit. Indeed it is possible to show for the case of E_F lying within the first miniband [rather than in the gap, as assumed in Eq. (47)] that the expression for the intraminiband mode is given by $\omega_{\text{intra}} = \Delta_1\{(me^2a/2\epsilon\hbar^4\pi)[k_Fa - \frac{1}{2}\sin(2k_Fa)]\}^{1/2}$. This expression reduces to the (isotropic) 3D result in the limit of $a \to 0$, and $\Delta_1 \to \infty$, while keeping $a^2\Delta_1 = 2\hbar^2/m$, so that the intraminiband plasmon becomes the well-known expression $\omega_{\text{intra}} \to (4\pi e^2 n_B/m\epsilon)^{1/2}$. Notice that for the parameters used, Eq. (53) yields $\omega_{\text{intra}} \approx 2.65$ meV, which is slightly shifted from the resonance feature in Fig. 2(a) (at 2.5 meV), due to the coupling between minibands ignored in (53).

Figure 2(b) shows $d_\perp$ for a superlattice with a finite number of periods but otherwise the same parameters as those in Fig. 2(a). We impose periodic boundary conditions on the wave functions to make the charge distribution uniform throughout and use five periods so the system has (nearly) the same total electronic density N_s as in the case with depletion discussed below. The collection of sharp peaks in $\text{Im}(d_\perp)$, produced by the discrete spacing of energy levels, clearly follows the overall shape of Fig. 2(a). In particular, the resonance frequency and line shape of the intraminiband plasmon are nearly the same for these two systems, showing that the "bulk" behavior is reached even for rather few layers in the structure.

Figure 2(c) shows $d_\perp$ for a ten-period system ($N = 10$) with the same Hamiltonian parameters as for Fig. 2(b) but now allowing charge depletion in the superlattice surface regions. Notice that due to the strong depletion of layers at both ends (approximately four and two on the free and buffer side, respectively), the effective number of populated layers is approximately five ($N_s = \sum_j \rho_j = 4.71\rho_+ a$). [This explains our choice above for a more quantitative comparison with the finite undepleted system of Fig. 2(b).] The intraminiband plasma frequency is basically the same, depending as it does on the tunneling probability in the system (Δ_1). Notice, however, that the intensity of the intraminiband plasmon in this system with depletion regions is slightly smaller than the results for the undepleted system, Fig. 2(b), due to the existence of additional excitations in the case of Fig. 2(c), which carry some of the total excitation strength. As the tunneling coefficient decreases, and the miniband widths are reduced, the resonant frequency of the intraminiband plasmon is shifted down. For example, if the miniband widths are reduced by half ($\Delta_1 = 1.24$ meV, $\Delta_2 = 5.20$ meV, and $E_{\text{gap}} = 31.0$ meV), the intraminiband plasmon is shifted to 1.2 meV, while its excitation strength is greatly decreased [see Fig. 2(d)]. This pattern of smaller excitation strength continues for still weaker tunneling systems, in agreement with the vanishing plasma frequency value of 2D systems, as discussed above.[10,22]

B. Interminiband excitations

In quantum-well systems as well as in superlattices with flat minibands (multiple-quantum-well limit), a collective excitation (i.e., a zero of the dielectric function) associated with interminiband energies is called an *interminiband plasmon*. Such a resonance can be viewed as a single-particle transition which has been shifted by the so-called depolarization effects. These shifts of the transition energies are proportional to a (dimensionless) Coulomb integral, called f, and to the effective volume charge density n_B,[42,48] such that the resonance frequency is given by $\omega^{(0)}_{\text{inter}} = (\omega_e^2 + f\omega_B^2)^{1/2}$, where ω_e is the interlevel separation, and $\omega_B = (4\pi e^2 n_B/m\epsilon)^{1/2}$ is the plasma frequency for the equivalent three-dimensional system ($n_B = N_s/a$). On the other hand, in the tunneling superlattices considered here, the miniband widths are comparable to the miniband gap, which causes significant changes in the spectrum of excitations of the system. As shown in Fig. 2(a), the single-particle excitations expected for $E_{\text{gap}} \le \hbar\omega \le E_{\text{gap}} + \Delta_1 + \Delta_2$ (i.e., $26 \le \hbar\omega \le 39$ meV) form a broad continuum, while the collective excitation yields a much stronger peak at a frequency $\omega_{\text{inter}} \approx 40$ meV, immediately following the edge of the single-particle continuum. This strong peak would be expected to dominate experimental excitation spectra, which indeed is observed in two-dimensional cases.[49–51]

In a finite superlattice system discrete peaks replace the single-particle interminiband continuum, as could be expected from the level "graininess" [Fig. 2(b) no depletion; 2(c) with depletion], although they follow the overall envelope of Fig. 2(a). The corresponding interminiband plasmon is shifted slightly to $\omega \approx 42$ meV. This difference is likely due to the ignored local field terms in the calculations of $\delta\epsilon_\perp$ above, while they are included to a degree in the tight-binding calculations of Eq. (38). The interminiband plasmon in the system with depletion regions of Fig. 2(c) is shifted even further (to 42.5 meV), and shows smaller intensity in comparison with the other finite-size system, an effect again of sharing the excitation strength with the surface-related modes.

As the bandwidths are reduced by half from those in Figs. 2(a)–2(c), the overall background related to the single-particle interminiband excitations becomes narrower (expected to lie between 31 and 37 meV) and weaker. However, the feature corresponding to the interminiband collective excitation becomes stronger, and approaches the behavior of a flat-miniband system, where it carries all of the excitation strength.[49–51] Notice also that the "relative depolarization shift" (defined as the separation between the interminiband plasmon and the upper edge of the single-particle background) increases

for the narrower bandwidth system, indicative of the observed larger effective oscillator strength, and expected in general for a more localized system.[42,45]

As mentioned before, in the results presented so far the semiconductor background was assumed to have a *static* dielectric constant $\epsilon_0 = 12.5$. This is a valid assumption for excitations occurring at frequencies far from the LO phonon ($\omega_L = 36.8$ meV). However, that is not the case for the interminiband transitions in the systems considered here, where $E_{gap} \approx 30$ meV. As an illustration of the possible effects, Fig. 3(a) shows $\mathrm{Im}(d_\perp)$ versus ω for the system with depletion regions of Fig. 2(c), when the dynamic electron-phonon coupling is restored by replacing the static dielectric constant with $\epsilon(\omega)$ of Eq. (39). Notice that all the electronic modes lying above the phonon resonance frequency are shifted upwards and enhanced due to the reduced screening by the background ($\epsilon_\infty = 10.4$). This is especially true for the interminiband plasmon, whose resonance frequency shifted to $\omega \approx 45$ meV since, as a result of the reduced screening, the effective electron-electron interaction increases, making depolarization effects stronger.

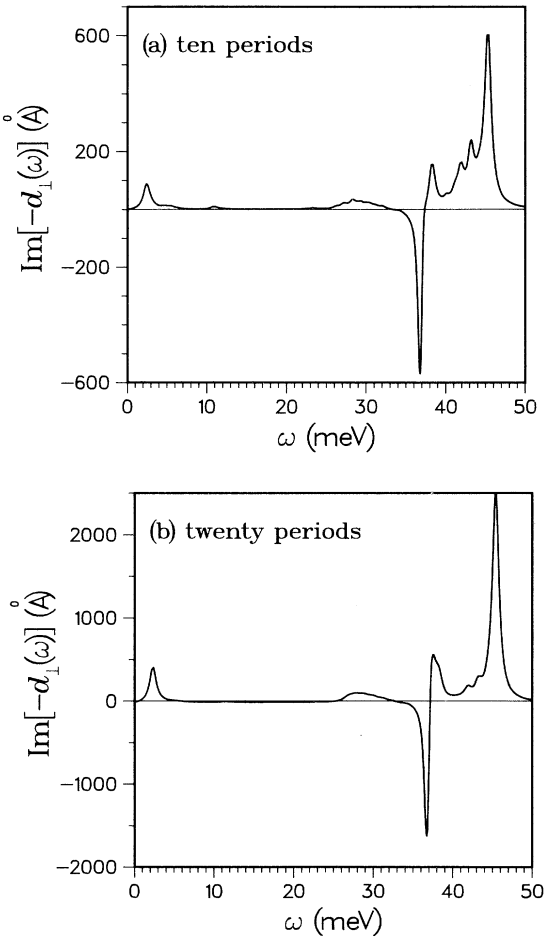

FIG. 3. (a) $\mathrm{Im}(d_\perp)$ vs frequency for ten-period system of Fig. 2(c), *with phonon dynamics included.* Two surface-depletion modes associated with each end of superlattice are distinguishable, $\omega \approx 42$ and 43 meV. (b) $d_\perp$ for twenty-period system with same parameters. Note scale change, as strength for "bulk" plasmons increases while intensity of surface-related modes remains constant.

For the most part, the spectrum corresponding to the interminiband single-particle excitations overlaps with the LO-phonon resonance, which appears as a strong peak in the opposite direction. This "negative" peak appears because the doped electrons present in the system would *reduce* the strong absorption of the dielectric background at that frequency. It is of course clear that by making use of the ability to change the electronic level structure over a wide range by varying a number of physical parameters (one of the main advantages of synthesized semiconductor systems), it would be possible to decouple the electron and phonon modes (by increasing E_{gap}, for example). Moreover, one could in principle also change miniband and gap parameters as the means to carefully study the electron-phonon mode coupling.[23–27,52] The d-parameter formalism could be used to study theoretically this phenomenon in a convenient fashion. Indeed, we have observed the anticipated anticrossing behavior of nearby modes for different structure parameters (not shown), with significant transfer of excitation strength taking place, especially in the case of crossing with the interminiband plasmon.

C. Surface modes

The most important differences between Figs. 2(a) and 2(b) and Fig. 2(c) are those features associated with the surface depletion regions present in a real system and described in the model of Sec. II B. These excitation modes in Fig. 2(c) are especially prominent as the structure in the absorption midgap ($\omega \approx 11$ meV), and in the shoulders of the intraminiband plasma peak and the interminiband broad background ($\omega \approx 5$ and 23 meV, respectively). These features arise from excitations between the minibands and the surface-localized states shown in Fig. 1 as dashed lines. The surface-depletion peaks in $\mathrm{Im}(d_\perp)$ have a dominant single-particle character, and are only slightly shifted from the corresponding transition energy by depolarization effects (≤ 0.5 meV). By analyzing the gate-voltage dependence of the level structure in Fig. 1, which is especially strong for surface-related states, one expects that the position of the midgap peak is rather easily changed by the applied gate voltages. During these voltage-driven shifts, moreover, the intensity of the peak remains fairly constant, an indication of its single-particle character with constant excitation strength.[4–9]

An important feature to notice in the depletion-region system is the strong peak at $\omega \approx 39.8$ meV in Fig. 2(c), which is absent in the curves for the bulk system. This strong feature (half as high as the interminiband plasmon

peak) is actually composed of two closely spaced peaks, resolved only for smaller values of the broadening parameter γ (= 1 meV here). These modes clearly possess interminiband character and large depolarization shifts, in analogy with the main collective-excitation peaks. We will see below that they are also characterized by peculiar oscillations of the induced charge density at these frequencies, with some similarities to the bulk modes.

As shown in Fig. 2(d), the position of the midgap surface-depletion peak for the narrower-band system is basically unchanged. The surface state giving rise to this transition has approximately the same energy with respect to the lower miniband in both cases, depending as it does mostly on the local potential values near the superlattice surface.

As the electron-phonon interactions are introduced in the calculation, Fig. 3(a), the high-frequency surface-depletion modes are enhanced and shifted to higher frequencies, similar to the interminiband plasmons, due to a weaker screening by the background. Furthermore, the two closely spaced surface modes in Fig. 2(c) are split and form clearly different peaks at $\omega \approx 42$ and 43.2 meV. Notice, however, that the surface-related features at lower frequencies are nearly unchanged, while their *relative* intensities are reduced in comparison with the interminiband plasmon peak.

In order to study the effects of system size on the surface-mode features, we have also calculated d parameters for a twenty-period system [Fig. 3(b)] with the same structural parameters as in Fig. 3(a). Since the depletion regions are situated within two or three layers near each end, increasing the total number of periods only increases the relative size of the bulklike region in the middle of the structure. This increases the ratio of extended to surface-localized states approximately as the bulk to surface ratio. As a result, the basic features in

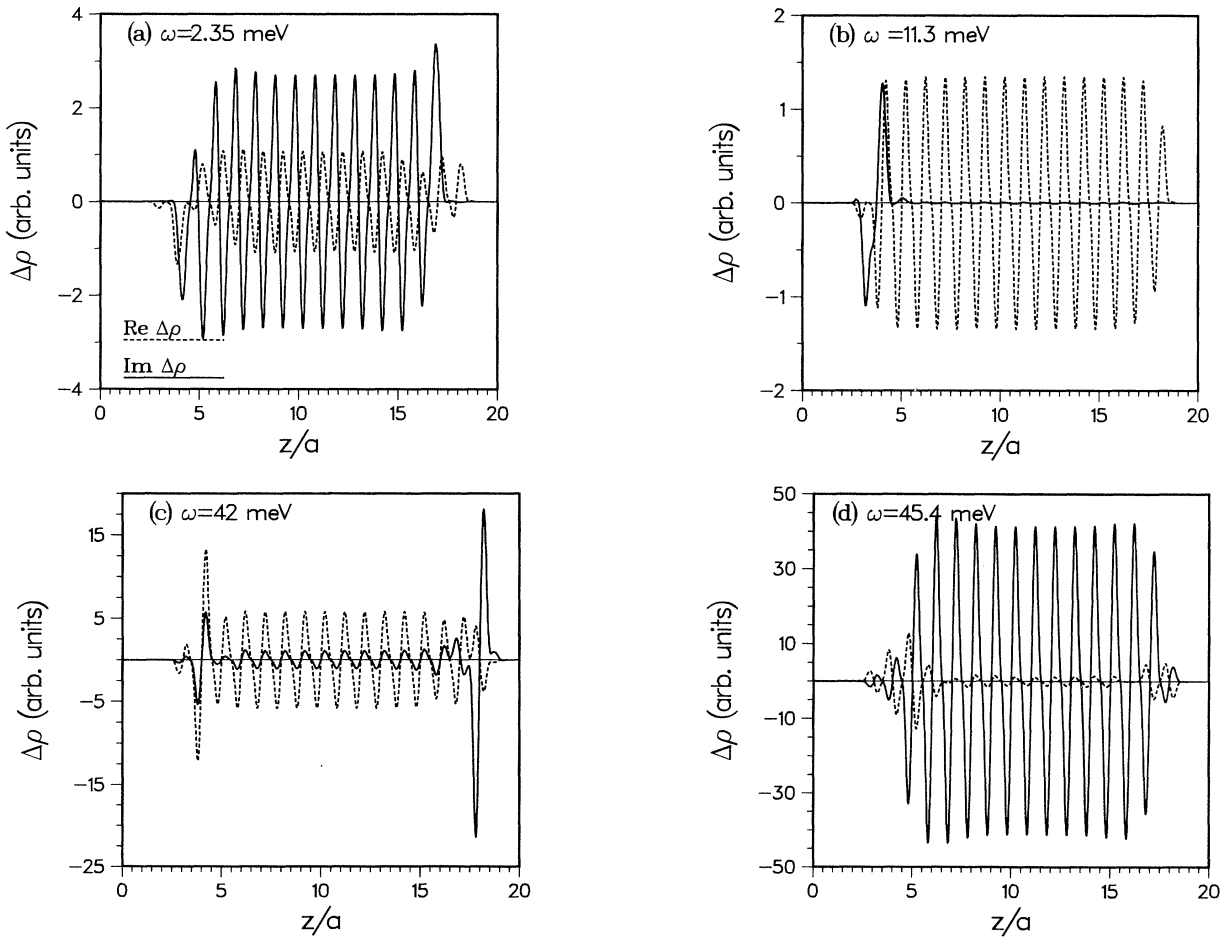

FIG. 4. Induced-charge-density distribution $\Delta\rho(z,\omega)$ for system of Fig. 3(b) at (a) $\omega = 2.35$ meV, (b) $\omega = 11.3$ meV, (c) $\omega = 42$ meV, and (d) $\omega = 45.4$ meV. Superlattice extends from free end ($z = 0$) to buffer ($z = 20a$). Notice surface modes, (b) and (c), showing dipolelike oscillations in depletion regions. Real (imaginary) part of $\Delta\rho$ shown dashed (solid) in all plots.

$d_\perp$ remain qualitatively the same, with the intensity of the intraminiband and interminiband plasma modes increasing, while the intensity of the surface modes remains unchanged. This is clear in the modes with $\omega \approx 42$ meV, while the mode at $\omega \approx 11$ meV is hardly visible (although still present) due to the scale change.

The different character of the surface-related modes may be further distinguished by inspection of the associated induced carrier density distribution of Eq. (37). Figure 4 shows induced carrier distributions $\Delta\rho(z,\omega)$ for the twenty-period system of Fig. 3(b), at resonant frequencies corresponding to two of the surface modes and to both the intraminiband and interminiband plasmons, all including the electron-phonon coupling. The imaginary part of $\Delta\rho$ for both plasma modes (at $\omega = 2.35$ and 45.4 meV) exhibits strong spatial oscillations of alternating sign which extend throughout the superlattice, while the corresponding real part shows smaller amplitudes [Figs. 4(a) and 4(d)]. Notice that the oscillations for ω_{intra} are much weaker than for ω_{inter}, an indication of their relative excitation strength. The strong density oscillations permeating the system at a resonance are reminiscent of similar behavior in metals.[34,53]

On the other hand, surface-depletion modes exhibit strong dipolelike structures in the imaginary part of $\Delta\rho$ near the end layers of the superlattice, which rapidly decay into the bulk region. For example, Fig. 4(b) shows the induced charge density at $\omega = 11.3$ meV, which corresponds to the midgap peak absorption [see Fig. 2(c)]. This $\text{Im}(\Delta\rho)$ exhibits its dipolelike feature near the free end of the superlattice, with a much weaker amplitude than the oscillations in the collective mode [contrast 4(b) and 4(d)]. Figure 4(c) shows the surface mode at $\omega = 42$ meV, which is related to the depletion region on the end attached to the buffer. This plot shows a dipolelike structure similar to that in Fig. 4(b), although small oscillations remain throughout the superlattice in this case. This is a signature of the bulklike contribution included in this surface-level–to–miniband transition. The mode at $\omega = 43.2$ meV (not shown), displays similar $\Delta\rho$ behavior but with the dipolar feature on the opposite (free) end of the structure. This explains the appearance of the doublet in $d_\perp$ as due to surface modes at each end of the superlattice.

Finally, since the various surface-related features appearing in $d_\perp$ are rather sensitive to the conditions of the surface, they are also strongly affected by applied gate voltages. In order to explore this sensitivity further, we plot in Fig. 5 the rate of change of $\text{Im}(d_\perp)$ with respect to gate voltage for both cases shown in Fig. 3. The gate voltage is assumed to be applied with respect to the layers in the middle of the structure such that it only affects the surface near the free end (which has now a gate deposited on it). Comparing the ten- and twenty-period results in Fig. 5, one finds that all the modes associated with the electron depletion in the "free" end appear as clear features in these curves, even those modes overlapped by "bulk" transitions and the phonon peak. The

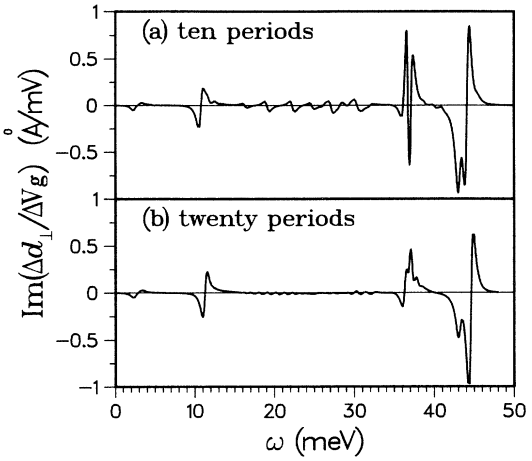

FIG. 5. Rate of change in $\text{Im}(d_\perp)$ with respect to gate voltage (about the point $V_{\text{gate}} = 0$) for the (a) ten-period and (b) twenty-period superlattices in Fig. 3. Large feature at 11 meV is due to miniband–to–surface-state midgap excitation.

large feature at $\omega \approx 43$ meV results from the depletion mode at that frequency, while that at $\omega \approx 45$ meV arises from a surface-to-surface interminiband transition. This excitation, which can be calculated from the energy levels in Fig. 1, is hidden in Fig. 2 by the interminiband plasmon. The midgap peak present at $\omega \approx 11$ meV gives rise to a noticeable feature. It is greatly enhanced by this differential technique, *regardless of the number of periods.* Notice also that the features appearing in the range 18–30 meV, which correspond to the shoulder and main part of the interminiband transitions, decrease in size but increase in number in the larger system. This is understandable since these excitations arise from surface to bulk (single-particle-like) transitions, and their overall excitation strength is then divided into more portions when the system increases in size. The significant enhancement of the various surface-related features by a gate voltage differential technique suggests utilizing it in the study of these systems. We would anticipate these experiments to need as much sophistication but to be as interesting as those performed in two-dimensional systems with similar techniques.[49–51]

D. Excitonic shifts

In the results presented so far, we have ignored the excitonic effects discussed in Sec. II C. As an illustration that this neglect is unimportant, we show in Fig. 6 the $\text{Im}(d_\perp)$ function resulting when $\mathbf{V}^x_{ss'}$ in Eq. (42) is included in the calculation of $d_\perp$, together with the corresponding change in the energy levels by including v^x_j in the Hamiltonian, for the system of Fig. 2(c). The corresponding curve without exchange effects included, Fig. 2(c), is also shown dashed. Neither curve includes phonon effects. It is clear that, as expected, the exchange

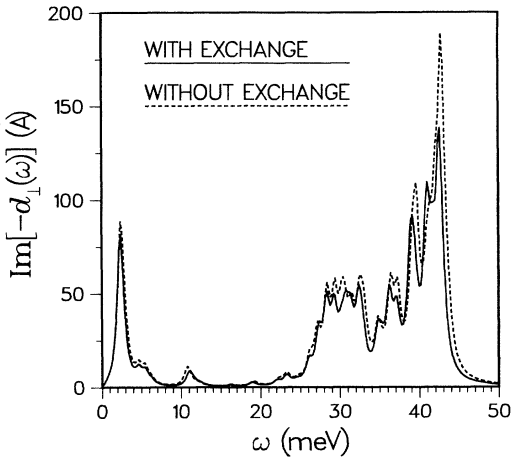

FIG. 6. Exchange potential effects on $d_\perp$ for the system in Fig. 2(c). Results of including both v_j^x and $\mathbf{V}^x_{ss'}$ (solid line) compared with results which neglect them (dashed line).

potential shifts back the excitation modes in the system, opposite to the depolarization up-shifts.[13,17,45] However, these excitonic shifts are much smaller than the corresponding depolarization ones, being typically less than 1 meV in this case. Perhaps more significant is the slight shift in strength between modes, although this does not produce qualitative changes in the relative intensities. [We also remark that the midgap peak at $\omega \simeq 11$ meV has been shifted up by exchange effects ($\simeq 0.2$ meV) but this is due to a shift of the originating surface-state level when v_j^x is included.]

IV. SUMMARY

We have used the d-parameter formalism to study the infrared absoption of doped tunneling semiconductor superlattices. The d parameters are determined by the systems' induced polarization in response to (nearly) uniform external fields and provide the excitation strengths of all modes that can be excited in this limit. The drastic changes in the electronic density profile in the depletion regions of the superlattice are incorporated in our calculation, and give rise to interesting surface modes. Some of these, with strong single-particle character, appear in the minigap region due to surface-localized Tamm superlattice states. Others, with stronger coupling strengths, are found to lie close to the bulk interminiband plasmon peak. Their location can be attributed to lower depolarization shifts associated with the reduced local density in the surface regions. The general sensitivity of the various surface-related modes to the details of the depletion profiles suggests that observations which simultaneously vary the gate voltage should allow one to control and identify these modes. Optical experiments in finite-size tunneling superlattice systems displaying these modes will be of great interest.

Our calculations have been directed towards quantitative measurements of infrared absorption but the basic ingredients can also be used to estimate signal strengths in other spectroscopies. We briefly indicate how this could be done and what additional features would appear. For inelastic scattering of either light[15–17,20] or electrons[54–58] the basic measureable quantity can be written as

$$P(\mathbf{Q},\omega) = \int dz \int dz'\, w(z)\, \mathrm{Im}\chi(z,z';\mathbf{Q},\omega)\, w(z'), \tag{54}$$

where $\mathbf{Q}$ is the wave-vector transfer parallel to the surface, and the weight factors $w(z)$ depend on the particular external probe being used. For electron-energy loss (via long-range dipole coupling), one has

$$w(z) = e^{-Qz}, \tag{55}$$

with $Q = |\mathbf{Q}|$, while for light scattering

$$w(z) = e^{i(p_i+p_s)z}, \tag{56}$$

where p_i and p_s are the normal components of the light's wave vector inside the substrate before and after the inelastic scattering, respectively. These w's should be contrasted to the simple factor of z leading to the H's of (38) which is the only surviving z dependence in the long-wavelength limit.

The susceptibility evaluated in Sec. II is the $\mathbf{Q} = 0$ limit of that required in (54). The latter can be analyzed in the same way as before if one formally includes a $\mathbf{Q}$ dependence in χ_0 and then in $\mathbf{V}$ and $\mathbf{B}$. For instance (24) and (25) change to

$$V_H(z,z';\mathbf{Q}) = \frac{2\pi e^2}{\epsilon Q} e^{-Q|z-z'|}, \tag{57}$$

$$V_I(z,z';\mathbf{Q}) = \frac{2\pi e^2}{\epsilon Q}\frac{\epsilon-1}{\epsilon+1} e^{-Q(z+z')}, \tag{58}$$

and the $\Pi_{n,n'}$ that determines $\mathbf{B}$ in (32) becomes

$$\Pi_{n,n'}(\mathbf{Q},\omega) = \frac{2}{A}\sum_{\mathbf{k}_t} \Theta(E_F - E_{n,\mathbf{k}_t}) \frac{2\left(E_n - E_{n'} - \frac{\hbar^2}{2m}(2\mathbf{k}_t\cdot\mathbf{Q} + Q^2)\right)}{\left(E_n - E_{n'} \frac{\hbar^2}{2m}(2\mathbf{k}_t\cdot\mathbf{Q} - Q^2)\right)^2 - \hbar\omega(\hbar\omega + i\gamma)}. \tag{59}$$

These various modifications do not change the mathematical structure of the calculation, but the different integrands will certainly lead to changes in the predicted spectra.

What should one expect on physical grounds? The response to parallel fields will undergo the greatest qualitative changes as one leaves the long-wavelength limit in that the various layers of the superlattice will cease to respond in phase and instead of the single plasmon described by (14) there will be a series of losses to a (developing) band of plasmons.[15,16,19,27] The surface effects of interest here would then influence the dispersion and coupling strength of these additional modes. Detailed calculations would be necessary to quantify this influence, such as have been done for electron energy loss from accumulation and depletion layers at the surfaces of (otherwise) homogeneous semiconductors.[54–58] Further numerical work would also be needed to learn how the interminiband excitations would change with increasing Q, but one can expect since couplings become of shorter range at larger Q that the sensitivity of the spectra to surface effects can be varied by changing the scattering configuration. Another degree of freedom that is available with inelastic light scattering arises from the polarization vectors of the propagating fields. By requiring the incident and scattered radiation to have orthogonal polarizations one can suppress the appearance of the Coulomb interactions described by (22) so the signal probes χ_0 alone. Such spectra can also be easily calculated. In summary, the use of alternative probes will provide complementary views of these systems and their analysis can be done in terms of a common physical picture using the quantities that underlie the calculational scheme developed here for infrared absorption.

ACKNOWLEDGMENTS

Calculations were performed on the Cray Research, Inc. computers at the Ohio Supercomputer Center. This work was supported by the U.S. Department of Energy (J.Z. and S.E.U.), Grant No. DE-FG02-91ER45334, and by the National Science Foundation (W.L.S.), Grant No. DMR 89-03851.

APPENDIX

The explicit Wannier functions needed in the calculation of the various matrix elements in the text were calculated numerically from the Bloch wave functions for a Kronig-Penney potential with the appropriate structure parameters (widths of well and barriers, and height of barrier). The Wannier function is defined by

$$\phi_j^\alpha(z) = \frac{a}{2\pi}\int e^{-ijka}\Psi_{k\alpha}(z)e^{i\gamma_\alpha(k)}\,dk, \tag{A1}$$

where $\Psi_{k\alpha}(z)$ is a Bloch function, α (j) is the band (site) index, k is a wave number within the first Brillouin zone, and $\gamma_\alpha(k)$ is a phase function. Because of the arbitrary phase of the Bloch states, one can see that Wannier functions are not uniquely determined, yielding functions which have entirely different localization properties. It is of course in our interest to find the phase function which produces the best localized Wannier state. A variational method which minimizes the normalization integral over a finite region of space (typically a unit cell) yields multiple solutions, some of them with very poor symmetry properties.[59] In fact, only one phase factor yields a real, well-localized, symmetric wave function in this one-dimensional problem, as discussed by Kohn.[43]

The Kronig-Penney potential was arranged to possess inversion symmetry, $V(z) = V(-z)$, and the phase factor $\gamma_\alpha(k)$ was chosen so as to reduce the integrand factor in Eq. (A1) at the origin,

$$\Psi_{k\alpha}(z=0)e^{i\gamma_\alpha(k)}, \tag{A2}$$

to a *real* number. This forces the conditions of Kohn's theorem to be satisfied and the resulting Wannier functions to be real, with definite symmetry (even for the first miniband, odd for the second, etc.), and well localized (97.9% of the normalization integral within a unit cell). In Fig. 7 we show the resulting Wannier functions for the first two minibands of a system with the same parameters as those in Fig. 2(a). As a consequence of the symmetries of ϕ_j^α, the dipole matrix elements between Wannier functions H_s in Eq. (55) can be shown to have a simple form. For the same-miniband case, they are given by

$$H_{(l,\alpha,j,\alpha)} = <\phi_l^\alpha \mid z \mid \phi_j^\alpha> = \int \phi_l^\alpha(z)\phi_j^\alpha(z)z\,dz = la\delta_{lj}. \tag{A3}$$

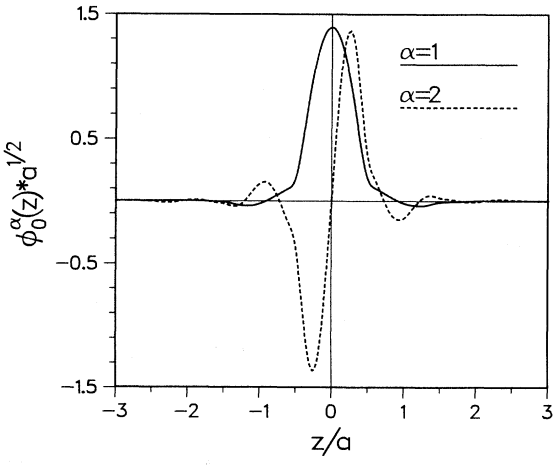

FIG. 7. Wannier states for a Kronig-Penney model with parameters as in Fig. 2(a). Solid (dashed) line shows function for the first (second) band ϕ_0^1 (ϕ_0^2).

For the interminiband transitions, on the other hand, one obtains numerically that $H_{(l,1,l,2)} = < \phi_l^1 \mid z \mid \phi_l^2 >= 0.1873a$ (same site), $H_{(l,1,l\pm1,2)} = -0.0365a$ (nearest neighbor), $H_{(l,1,l\pm2,2)} = 0.0048a$ (next-nearest neighbor), and quickly decaying (and oscillating) values thereafter. The rapidly converging series of dipole matrix elements is a by-product of the optimal localization of the Wannier function. This allows one to keep the various matrices involved in the calculations of the response functions relatively small. Indeed, the matrix elements of $\mathbf{V}$, $\mathbf{B}$, and $\mathbf{C}^l$ beyond nearest neighbors proved to be negligible in the calculations of the different excitation modes.

[1] For recent reviews, see, for example, L. Esaki, IEEE J. Quantum Electron. **QE-22**, 1611 (1986); P. J. Stiles, in *Interfaces, Quantum Wells and Superlattices*, Vol. 179 of *NATO Advanced Study Institute, Series B: Physics*, edited by C. R. Leavens and R. Taylor (Plenum, New York, 1988), p. 1.

[2] S. E. Ulloa and G. Kirczenow, Phys. Rev. Lett. **57**, 2991 (1986).

[3] S. E. Ulloa and G. Kirczenow, Phys. Rev. B **37**, 8337 (1988).

[4] J. Zhang and S. E. Ulloa, Phys. Rev. B **38**,2063 (1988).

[5] J. Zhang and S. E. Ulloa, Solid State Commun. **71**, 643 (1989).

[6] J. Zhang, Y. S. Joe, and S. E. Ulloa, Surf. Sci. **228**, 422 (1990).

[7] Y. S. Joe and S. E. Ulloa, J. Phys. Condens. Matter **2**, 7137 (1990).

[8] J. Zhang and S. E. Ulloa, Surf. Sci. **229**, 415 (1990).

[9] J. Zhang, S. E. Ulloa, and W. L. Schaich, Phys. Rev. B **41**, 5467 (1990).

[10] D. Grecu, Phys. Rev. B **8**, 1958 (1973).

[11] A. L. Fetter, Ann. Phys. (N.Y.) **81**, 367 (1973); **88**, 1 (1974).

[12] S. Das Sarma and J. J. Quinn, Phys. Rev. B **25**, 7603 (1982).

[13] A. C. Tselis and J. J. Quinn, Phys. Rev. B **29**, 3318 (1984).

[14] S. Das Sarma, Phys. Rev. B **29**, 2334 (1984).

[15] J. K. Jain and P. B. Allen, Phys. Rev. Lett. **54**, 947 (1985); **54**, 2437 (1985); Phys. Rev. B **32**, 997 (1985).

[16] P. Hawrylak, J. W. Wu, and J. J. Quinn, Phys. Rev. B **32**, 5169 (1985).

[17] S. Katayama and T. Ando, J. Phys. Soc. Jpn. **54**, 1615 (1985).

[18] R. D. King-Smith and J. C. Inkson, Phys. Rev. B **33**, 5489 (1986).

[19] J. K. Jain and S. Das Sarma, Phys. Rev. B **35**, 918 (1987).

[20] G. Eliasson, P. Hawrylak, and J. J. Quinn, **35**, 5569 (1987).

[21] G. F. Giuliani, P. Hawrylak, and J. J. Quinn, Phys. Scr. **36**, 946 (1987).

[22] X. Zhu, X. Xia, J. J. Quinn, and P. Hawrylak, Phys. Rev. B **38**, 5617 (1988).

[23] D. Olego, A. Pinczuk, A. C. Gossard, and W. Wiegmann, Phys. Rev. B **25**, 7867 (1982).

[24] R. Sooryakumar, A. Pinczuk, A. C. Gossard, and W. Wiegmann, Phys. Rev. B **31**, 2578 (1985).

[25] A. Pinczuk, M. G. Lamont, and A. C. Gossard, Phys. Rev. Lett. **56**, 2092 (1986).

[26] G. Fasol, N. Mestres, H. P. Hughes, A. Fischer, and K. Ploog, Phys. Rev. Lett. **56**, 2517 (1986).

[27] A. Pinczuk and G. Abstreiter, in *Light Scattering in Solids V*, edited by M. Cardona and G. Güntherodt (Springer, New York, 1989), p. 153.

[28] P. Apell, Phys. Scr. **24**, 795 (1981).

[29] P. J. Feibelman, Prog. Surf. Sci. **12**, 287 (1982).

[30] P. Apell, A. Lyungbert, and S. Lundqvist, Phys. Scr. **30**, 367 (1984).

[31] F. Forstmann and R. R. Gerhardts, *Metal Optics Near the Plasma Frequency* (Springer, Berlin, 1986).

[32] K.-D. Tsuei, E. W. Plummer, and P. J. Feibelman, Phys. Rev. Lett. **63**, 2256 (1989).

[33] K.-D. Tsuei, E. W. Plummer, A. Liebsch, K. Kempa, and P. Bakshi, Phys. Rev. Lett. **64**, 44 (1990).

[34] K. Kempa, A. Liebsch, and W. L. Schaich, Phys. Rev. B **38**, 12 645 (1988).

[35] D. C. Langreth, Phys. Rev. B **39**, 10 020 (1989).

[36] W. L. Schaich and Wei Chen, Phys. Rev. B **39**, 10 714 (1989).

[37] K. Kempa, D. A. Broido, C. Beckwith, and J. Cen, Phys. Rev. B **40**, 8385 (1989).

[38] Z. Y. Zhang and D. C. Langreth, Phys. Rev. B **39**, 10 028 (1989).

[39] Wei Chen and W. L. Schaich, Surf. Sci. **218**, 580 (1989); **220**, L733 (1989).

[40] We assume that magnetic polarization is negligible: $\mu = 1$.

[41] C. H. Wu and W. Hanke, Solid State Commun. **23**, 829 (1977).

[42] D. A. Dahl and L. J. Sham, Phys. Rev. B **16**, 651 (1977).

[43] W. Kohn, Phys. Rev. **115**, 809 (1959).

[44] L. Hedin and B. I. Lundqvist, J. Phys. C **4**, 2064 (1971).

[45] T. Ando, Z. Phys. B **26**, 263 (1977).

[46] N. Wiser, Phys. Rev. **129**, 62 (1963).

[47] H. L. Störmer, J. P. Eisenstein, A. C. Gossard, W. Wiegmann, and K. Baldwin, Phys. Rev. Lett. **56**, 85 (1986).

[48] S. J. Allen, Jr., D. C. Tsui, and B. Vinter, Solid State Commun. **20**, 425 (1976).

[49] E. Batke, D. Heitmann, and C. W. Tu, Phys. Rev. B **34**, 6951 (1986).

[50] M. J. Kane, M. T. Emery, N. Apsley, E. R. Whitehouse, and D. Lee, Superlatt. Microstruct. **5**, 587 (1989).

[51] N. Schwarz, F. Müller, G. Tempel, F. Koch, and G. Weimann, Semicond. Sci. Technol. **4**, 571 (1989).

[52] A. Pinczuk, J. M. Worlock, H. L. Störmer, R. Dingle, W. Wiegmann, and A. C. Gossard, Solid State Commun. **36**, 43 (1980).

[53] A. Liebsch, Phys. Rev. B **36**, 7378 (1987).

[54] D. H. Ehlers and D. L. Mills, Phys. Rev. B **36**, 1051 (1987).

[55] S. R. Streight and D. L. Mills, Phys. Rev. B **38**, 8526 (1988).

[56] S. R. Streight and D. L. Mills, Phys. Rev. B **40**, 10 488 (1989).

[57] H. Yu and J. C. Hermanson, Phys. Rev. B **40**, 11 851 (1989).

[58] H. Yu and J. C. Hermanson, Phys. Rev. B **41**, 5991 (1990).

[59] M. Kertesz and G. Biczo, Phys. Status Solidi B **60**, 249 (1973).